Optics Letters

Polarization-independent photonic Bragg grating filter with cladding asymmetry

Daniel Pimbi,[1,2] Mehedi Hasan,[1,2] Md Borhan Mia,[1,2] Nafiz Jaidye,[2,3] and Sangsik Kim[1,2,3,4,*]

[1] Department of Electrical and Computer Engineering, Texas Tech University, Lubbock, Texas 79409, USA
[2] Nano Tech Center, Texas Tech University, Lubbock, Texas 79409, USA
[3] Department of Physics and Astronomy, Texas Tech University, Lubbock, Texas 79409, USA
[4] School of Electrical Engineering, Korea Advanced Institute of Science and Technology, Daejeon 34141, Republic of Korea
*Corresponding author: sangsik.kim@kaist.ac.kr

Received 28 October 2022; revised 19 January 2023; accepted 23 January 2023; posted 24 January 2023; published 22 February 2023

A photonic Bragg grating is a fundamental building block that reflects the direction of wave propagation through spatial phase modulation and can be implemented using sidewall corrugation. However, due to the asymmetric aspect ratio of a waveguide cross section, typical Bragg gratings exhibit a strong polarization sensitivity. Here, we show that photonic Bragg gratings with cladding asymmetry can enable polarization-independent notch filters by rotating input polarizations. Such Bragg gratings strongly couple transverse electric (TE) and transverse magnetic (TM) modes propagating in opposite directions, filtering the input signal and reflecting the rotated mode. We analyzed this polarization-rotating Bragg grating using the coupled-mode theory and experimentally demonstrated it on a silicon-on-insulator platform. Our device concept is simple to implement and compatible with other platforms, readily available as polarization transparent Bragg components.

https://doi.org/10.1364/OL.479600

A Bragg grating is a distributed reflector consisting of a periodic structure such that the spatial phase modulation reflects the input waves [1–3]. At the Bragg condition, multiple reflections from each periodic boundary interfere constructively, forming a strong and narrow reflection band centered at a wavelength, namely the Bragg wavelength. At wavelengths other than the Bragg condition, the reflected lights interfere destructively due to phase mismatching, resulting in the input light being transmitted through the gratings. As a result, Bragg gratings function as notch filters. In integrated photonics, Bragg gratings are implemented using either sidewall corrugation in the waveguide core (i.e., by changing the waveguide width or height) [1–3] or periodic grating patterns in the cladding [4,5]. Bragg gratings have been utilized for a wide range of advanced applications, including spectral filtering [4], pulse shaping [6], dispersion compensation [7], wavelength division multiplexing [8], and optical signal processing [9]. However, photonic Bragg grating is intrinsically sensitive to polarizations due to their different modal indices, matching the Bragg condition at different wavelengths. This polarization dependency of a Bragg grating limits the system to being operated only at a single polarization. The size of a Bragg grating is typically large (as its reflectivity increases per number of periods); thus, having separate Bragg gratings for transverse electric (TE) and transverse magnetic (TM) modes increases the system size and complexity drastically, which is detrimental to the whole system.

One approach to making the Bragg grating insensitive to input polarization is matching the effective indices of TE and TM modes [10–12]. Various approaches can be considered to achieve this, such as symmetric waveguide height and width [10], cross-slot waveguide [11], and index engineering via subwavelength gratings [12]. However, such an approach would still cause different reflection coefficients for each polarization, resulting in different extinction ratios and bandwidths while matching the Bragg wavelength. Alternatively, polarization-rotating Bragg gratings can be established, which naturally achieve polarization-insensitive filtering [13–17]. By making the grating cross sections asymmetric, one can strongly couple TE and TM modes; then, both modes can be used to satisfy the Bragg condition regardless of the input polarization. Breaking the vertical symmetry is the key to implementing this, but most approaches used double etching or angled sidewall, adding more complexity to the process with low accuracy.

In this paper, we show that single-etched photonic Bragg gratings with cladding asymmetry can effectively achieve polarization-independent Bragg filtering. We use air cladding to introduce the cladding asymmetry on a single-etched monolithic device, efficiently coupling TE and TM modes for polarization rotation. The Bragg condition is satisfied at the average of TE and TM modes, filtering the input polarization mode and reflecting the rotated mode. We use coupled mode theory to design our Bragg gratings and to quantify the coupling strength between TE and TM modes. We experimentally demonstrate this on a single-etched 220 nm thick silicon-on-insulator (SOI) platform, confirming its polarization-independent Bragg filtering. Figure 1(a) shows the schematic of the proposed polarization-independent photonic Bragg grating. Red and gray represent Si and SiO_2, respectively. The Bragg gratings are designed by alternating a simple rectangular strip waveguide (height $h = 220$ nm

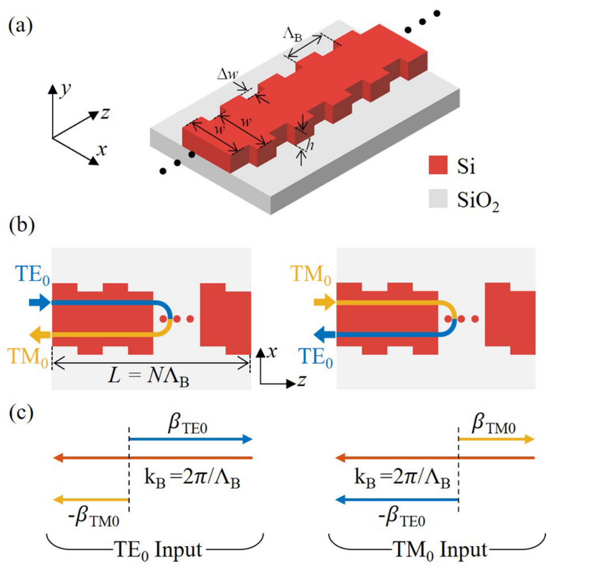

Fig. 1. (a) Schematic view of the proposed polarization-independent Bragg grating with cladding asymmetry: Si (red) and SiO_2 (gray). (b) Top view of the gratings, illustrating the polarization rotation and reflection at the Bragg condition (left, TE_0 input; right, TM_0 input). The waveguide height and width are $h = 220$ nm and $w = 450$ nm, respectively, with the corrugation depth $\Delta w = 50$ nm. The Bragg periodicity and the number of periods are $\Lambda_B = 390$–420 nm and $N = 100$–500, respectively. (c) Phase diagrams of the polarization rotating Bragg reflection: left, TE_0 input; right, TM_0 input.

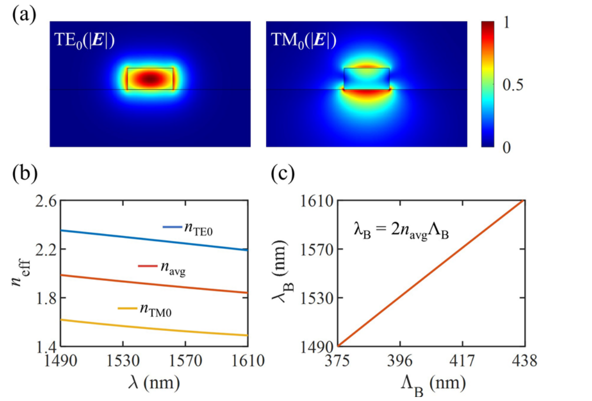

Fig. 2. (a) Normalized electric field profiles ($|\boldsymbol{E}|$) of the strip waveguide: TE_0 (left) and TM_0 (right) modes. (b) Simulated effective refractive indices of the TE_0 (n_{TE0}, blue) and TM_0 (n_{TM0}, yellow) modes. The orange line represents the average n_{avg} between n_{TE0} and n_{TM0}. (c) Theoretical estimate of the Bragg wavelength λ_B as a function of the Bragg period Λ_B, using Eq. (2).

and width $w = 450$ nm) with a corrugation offset $\Delta w = 50$ nm and the Bragg periodicity $\Lambda_B = 390$–420 nm. Air cladding is presented, introducing vertical cladding asymmetry. The number of periods ranges $N = 100$–500, and the total device length is $L = N \cdot \Lambda_B$. Figure 1(b) shows the top view of the Bragg grating, illustrating the polarization rotation and reflection with the fundamental TE (TE_0, left) and TM (TM_0, right) inputs at the Bragg condition. Figure 1(c) shows the corresponding phase diagrams, satisfying the Bragg conditions with polarization rotations: TE_0 (left) and TM_0 (right) inputs. Notice that, regardless of the input polarization, the Bragg condition satisfies

$$\Delta\beta = \beta_{TE0} - (-\beta_{TM0}) - \frac{2\pi}{\Lambda_B} = 0, \tag{1}$$

where β_{TE0} and β_{TM0} represent the propagation constants for the TE_0 and TM_0 modes, respectively. The magnitude of the propagation constant β_{TE0} is typically larger than β_{TM0}, since TE_0 has a larger effective index with a higher field confinement. This is also depicted in Fig. 1(c). By inserting $\beta_{TE0} = (2\pi n_{TE0})/\lambda_B$ and $\beta_{TM0} = (2\pi n_{TM0})/\lambda_B$ into Eq. (1), we can obtain the Bragg wavelength λ_B at which the reflection is maximum,

$$\lambda_B = (n_{TE0} + n_{TM0})\Lambda_B = 2n_{avg}\Lambda_B, \tag{2}$$

where $n_{avg} = (n_{TE0} + n_{TM0})/2$ is the average effective index between the n_{TE0} and n_{TM0}. Notice that all the effective indices $n_{TE0}(\lambda_B)$, $n_{TM0}(\lambda_B)$, and $n_{avg}(\lambda_B)$ are as a function of wavelength; thus, Eq. (2) should be solved numerically. To find out the Bragg periodicity Λ_B associated with the Bragg wavelength λ_B near the telecommunication band, we simulated the modal properties of TE_0 and TM_0. Figure 2(a) shows the simulated mode profiles $|\boldsymbol{E}|$ of TE_0 (left) and TM_0 (right) modes, and Fig. 2(b) shows their effective refractive indices as a function of wavelength for TE_0 (solid blue line) and TM_0 (solid yellow line). The average effective index n_{avg} is also plotted with a solid orange line. We numerically solved Eq. (2) using the graphical method, and Fig. 2(c) presents the theoretically estimated Bragg wavelength as a function of the Bragg period. Based on this, we chose the Bragg periodicity in the range of $\Lambda_B = 390$–420 nm, having λ_B near 1550 nm. Note that, since our Bragg grating has identical cross sections in each layer, this estimate is independent of the corrugation offset Δw and gives a good prediction for the Bragg wavelength.

To confirm the Bragg wavelength estimations and assess its polarization-independency, we analyzed our Bragg gratings using the coupled-mode theory (CMT). First, we ran the modal simulations and calculated the coupling coefficients κ_x, κ_y, and κ_z, given by [1]

$$\kappa_i = \frac{\omega\varepsilon_0}{4} b_m \iint E_{1i}^*(x, y) \cdot \Delta\varepsilon_i(x, y) E_{2i}(x, y) \mathrm{d}x\mathrm{d}y, \tag{3}$$

where the subscript $i = x, y$, and z. The b_m is the Fourier expansion coefficient of the periodic waveguide grating. The $\Delta\varepsilon_i$ denotes the dielectric perturbation due to the sidewall corrugation Δw. The $E_{1i}(x, y)$ and $E_{2i}(x, y)$ are normalized electric fields of the two interacting modes, here the subscripts 1 and 2 represent TE_0 and TM_0 modes, respectively. The overall coupling coefficient can be represented by adding the coefficients from each field component, i.e., $|\kappa| = |\kappa_x + \kappa_y + \kappa_z|$. Figure 3(a) shows the magnitude of the calculated coupling coefficients: $|\kappa_{11}|$ (purple dashed) and $|\kappa_{22}|$ (yellow dashed) represent the TE_0 to TE_0 and TM_0 to TM_0 couplings, respectively, and $|\kappa_{12}| = |\kappa_{21}^*|$ (blue solid) represents the coupling between TE_0 and TM_0 modes. Notice the high coupling coefficient between TE_0 and TM_0 modes (i.e., $|\kappa_{12}| = |\kappa_{21}^*|$) compared with others. This clearly indicates the strong coupling between TE_0 and TM_0 modes, which means the rotation of polarizations through this Bragg grating. The κ_{11} and κ_{22} are very low ($<10\ \mathrm{m}^{-1}$), avoiding the side Bragg responses from TE_0 to TE_0 and TM_0 to TM_0 couplings (see Supplement 1).

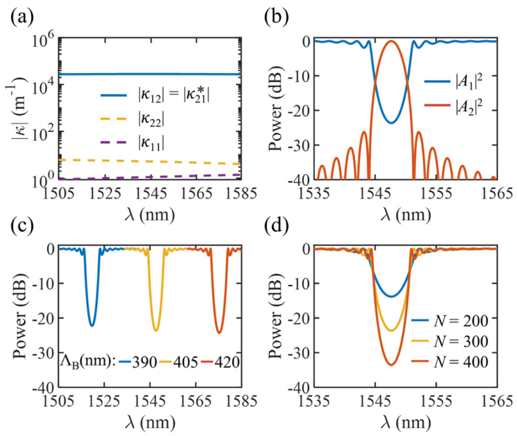

Fig. 3. (a) Calculated coupling coefficients using Eq. (3). The solid blue line represents the coupling coefficient between TE_0 and TM_0 modes ($|\kappa_{12}| = |\kappa_{21}^*|$). The dashed yellow and purple lines are the coupling coefficients of TM_0 to TM_0 ($|\kappa_{22}|$) and TE_0 to TE_0 ($|\kappa_{11}|$) modes, respectively. (b) Calculated transmission $|A_1|^2$ and reflection $|A_2|^2$ using Eq. (4) (Λ_B = 405 nm and N = 300). Similar transmission spectra while varying (c) the periodicity Λ_B = 390 (blue), 405 (yellow), and 420 (orange) nm (fixing the N = 300) and (d) the number of periods N = 200 (blue), 300 (yellow), and 400 (orange) (fixing the Λ_B = 405 nm). Other parameters are the same as in Fig. 1.

Using these coupling coefficients, we numerically calculated the following coupled-mode equations [1]:

$$\frac{d}{dz}A_1 = -i\kappa_{12}A_2(z)e^{i\Delta\beta z},$$
$$\frac{d}{dz}A_2 = i\kappa_{21}A_1(z)e^{-i\Delta\beta z}, \tag{4}$$

where, A_1 and A_2 are the amplitudes of the forward (input) and backward (reflected) propagating modes, respectively. Note that the phase difference $\Delta\beta$ is from Eq. (1) and zero at the Bragg wavelength, achieving the peak reflection. Figure 3(b) shows the calculated transmission $|A_1|^2$ (blue) and reflection $|A_2|^2$ (orange) spectra using Eq. (4) when Λ_B = 405 nm and N = 300. Other parameters are the same as described in Fig. 1, unless otherwise addressed. Since the Bragg wavelength appears at the average of TE_0 and TM_0 and the coupling coefficients are the same, exciting TE_0 or TM_0 would not differ in spectral response, i.e., polarization independent. Furthermore, as expected, the peak reflection appears at ≈ 1548 nm, which matches with Fig. 2(c). Changing the grating period ±15 nm shifts the Bragg wavelength approximately to ±28 nm, as shown in Fig. 3(c). The total number of periods N would not affect the Bragg wavelength's spectral location, but it defines the degree of reflection, i.e., peak reflection and spectral sharpness. The transmission spectra varying N = 200, 300, and 400 are shown in Fig. 3(d), increasing the degree of reflection as N increases. We then fabricated our devices on an SOI wafer comprising a 220 nm thick Si layer and a 2 μm thick SiO_2 layer. Electron beam lithography was used to define the device patterns. We fabricated two sets of devices with TE and TM grating couplers to ensure polarization status during the characterization. Figure 4(a) shows the scanning electron microscope images of the fabricated device set with the zoomed-in image showing the Bragg gratings.

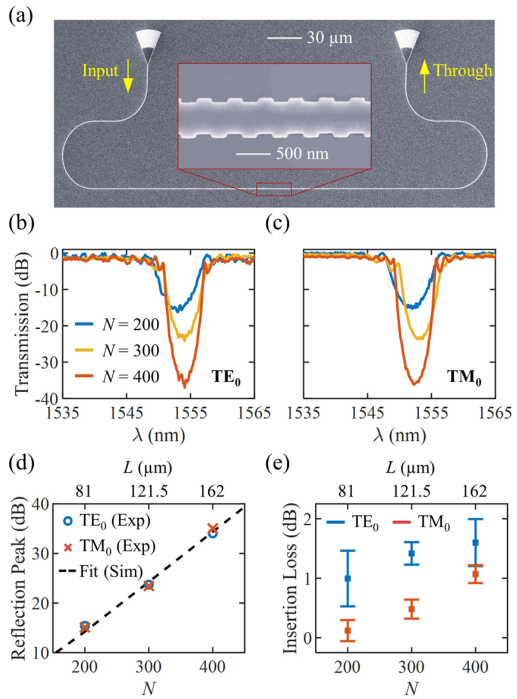

Fig. 4. (a) Scanning electron microscope image of the fabricated device (zoomed-in image: Bragg grating). Experimentally characterized transmission spectra for (b) TE_0 and (c) TM_0 inputs: N = 200 (blue); 300 (yellow); and 400 (orange). The Bragg periodicity is fixed at Λ_B = 405 nm. (d) Extracted peak reflections for different N and L: TE_0 (blue circles) and TM_0 (orange crosses) inputs. Black dashed line is the numerical result. (e) Insertion losses for different N and L: TE_0 (blue) and TM_0 (orange).

We characterized the devices using a custom-built grating coupler setup with a tunable laser source and an optical power meter. A polarization controller was connected after the laser source, controlling the input polarization. The calibration devices without Bragg structures were also fabricated and used to normalize the spectra. Figures 4(b) and 4(c) show the measured transmissions for TE_0 and TM_0 inputs, respectively, when Λ_B = 405 nm. Different colors represent the different number of periods N = 200 (blue), 300 (yellow), and 400 (orange). Notice that both TE_0 and TM_0 transmissions show almost identical spectra, having Bragg wavelengths differ only approximately $\Delta\lambda_B \approx 0.1$–0.7 nm. We fabricated identical designs on two different chips, having TE_0 and TM_0 grating couplers. These different environments might cause a difference in λ_B, but we expect more identical spectra if we measure them within one chip. Since the number of period is less sensitive between chip-to-chip variations, the peak extinction ratios of the reflection are close, having <1.1 dB difference between TE_0 and TM_0 data. These also match well with the simulated results in Fig. 3(d). The experimentally measured reflection peaks for TE_0 (blue circles) and TM_0 (orange crosses) are extracted in Fig. 4(d), providing excellent agreements with the simulated result (black dashed line). The insertion losses of the devices are also characterized in Fig. 4(e), by taking averages and standard deviations of off-Bragg wavelength transmissions. The uncertainty is mostly from grating coupler characterizing setup.

Figures 5(a) and 5(b) show the measured transmission spectra for TE_0 and TM_0 inputs, respectively, similar to Figs. 4(a) and

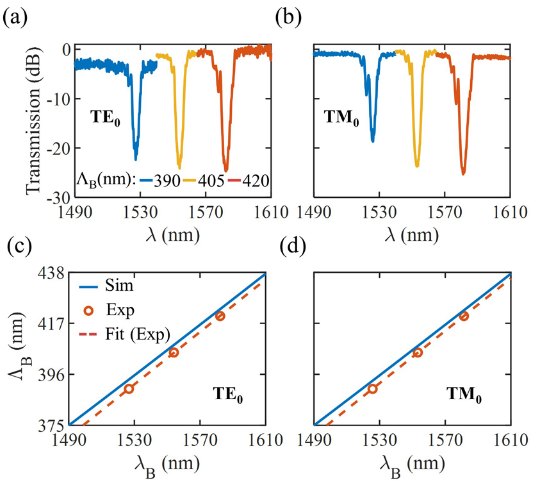

Fig. 5. Experimentally characterized transmission spectra for (a) TE_0 and (b) TM_0 inputs at different Λ_B = 390 (blue), 405 (yellow), and 420 (orange) nm. The Bragg periodicity is fixed at N = 300. Extracted Bragg wavelength λ_B for each Bragg period Λ_B (orange circles): (c) TE_0 and (d) TM_0 inputs. The orange dashed lines are their fitting lines. The blue lines are numerical results from Fig. 2(c).

Table 1. Summary of the Previously Reported Polarization-independent Photonic Bragg Gratings[a]

Cladding asymmetry	FWHM (nm)	*ER* (dB)	*L* (μm)
Angled sidewall [13]	1.5	18	1000
Double etch [15]	10	15	500
Double etch [17]	8	22	470
Double etch [16]	0.2	22	331
Double etch [14]	2.63	27	300
Single etch (this work)	**≈ 6**	**≈ 34**	**162**

[a]FWHM (full width at half maximum), *ER* (extinction ratio at peak reflection), *L* (device length).

4(b) but with different Λ_B, demonstrating Fig. 3(c). We also replot the numerically estimated Λ_B versus λ_B (solid blue line) and compare it with extracted λ_B (orange circles) in Figs. 5(c) and 5(d). The dashed orange line indicates the fitting line for the experimental data. The measured λ_B slightly redshifted ≈ 6 nm compared with the simulation results, probably due to fabrication imperfections and wafer non-uniformity. However, between TE_0 and TM_0, the characterized λ_B agrees well within ≈ 1.5 nm wavelength, confirming its polarization independency.

Table 1 summarizes the previously reported polarization-independent Bragg filters, including this work. While most approaches utilized double-etching or angled sidewall for breaking the vertical symmetry, our asymmetric cladding approach can use single-etched monolithic PICs. We report polarization-independent Bragg filters with extinction ratios ≈ 34 dB and full width at half maximum (FWHM) bandwidth ≈ 6 nm for a 162 μm-long device, which also can be engineered further by changing the Δw and N. Furthermore, while we used an air cladding to introduce the concept, the cladding asymmetry also can be implemented using other cladding materials such as low-index polymers. The same design methodology introduced here can be applied to designing polarization-independent Bragg filters, probably requiring more number of Bragg periods due to less index contrast.

In conclusion, we have proposed and experimentally demonstrated polarization-independent Bragg gratings by rotating input polarizations with cladding asymmetry. The cladding asymmetry is introduced on an SOI platform using air cladding, which can also be replaced by other low-index claddings or index-matching fluids. We designed our Bragg grating by alternating the same cross section strip waveguides with a fixed corrugation offset, which is simple to design and fabricate using a single-etching process. In support of the strong coupling between TE_0 and TM_0 modes, our device offers a compact length, achieving ≈ 15–34 dB extinction ratios and ≈ 6–8 nm FWHM for 81–162 μm-long gratings. Demonstrated on a widely used SOI, our polarization-independent Bragg grating is readily available for advanced PICs, and the same concept can be easily applicable to other platforms and spectral regimes.

Funding. National Science Foundation (1930784, 2144568); Korea Advanced Institute of Science and Technology (G04220043); U.S. Department of Energy (DE-NA-0003525); Korean-American Scientists and Engineers Association.

Acknowledgments. This work was performed, in part, at the Center for Integrated Nanotechnologies (CINT), an Office of Science User Facility operated for the U.S. Department of Energy Office of Science by Los Alamos National Laboratory and Sandia National Laboratories.

Disclosures. The authors declare no conflicts of interest.

Data availability. Data underlying the results presented in this paper may be obtained from the authors upon reasonable request.

Supplemental document. See Supplement 1 for supporting content.

REFERENCES

1. A. Yariv and P. Yeh, *Photonics: Optical Electronics in Modern Communications* (Oxford University Press, 2007).
2. J. Buus, M.-C. Amann, and D. J. Blumenthal, *Tunable Laser Diodes and Related Optical Sources* (John Wiley & Sons, 2005).
3. X. Wang, "Silicon photonic waveguide Bragg gratings," Ph.D. thesis, University of British Columbia (2013).
4. D. Pereira-Martín, J. M. Luque-González, J. G. Wangüemert-Pérez, A. Hadij-ElHouati, I. Molina-Fernández, P. Cheben, J. H. Schmid, S. Wang, W. N. Ye, J. Čtyroký, and A. Ortega-Moñux, Opt. Express **29**, 15867 (2021).
5. P. Cheben, J. Čtyroký, J. H. Schmid, S. Wang, J. Lapointe, J. G. Wangüemert-Pérez, I. Molina-Fernández, A. Ortega-Moñux, R. Halir, D. Melati, D. Xu, S. Janz, and M. Dado, Opt. Lett. **44**, 1043 (2019).
6. M. Martyanov, I. Mukhin, I. Kuzmin, and S. Mironov, Opt. Lett. **47**, 557 (2022).
7. C. Klitis, M. Sorel, and M. J. Strain, Micromachines **10**, 569 (2019).
8. A. D'Orazio, M. D. Sario, V. Petruzzelli, and F. Prudenzano, Opt. Express **11**, 230 (2003).
9. W. Zhang and J. Yao, Nat. Commun. **9**, 1396 (2018).
10. H. Okayama, Y. Onawa, D. Shimura, H. Takahashi, S. Miyamura, H. Yaegashi, and H. Sasaki, Electron. Lett. **50**, 388 (2014).
11. M. Roussey, P. Stenberg, A. Bera, S. Paul, J. Tervo, M. Kuittinen, and S. Honkanen, Opt. Express **22**, 24149 (2014).
12. H. Sun and L. R. Chen, in *Conference on Lasers and Electro-Optics*, (2022), p. JW3B.14.
13. H. Okayama, Y. Onawa, D. Shimura, H. Yaegashi, and H. Sasaki, Opt. Express **22**, 31371 (2014).
14. H. Yun, Z. Chen, Y. Wang, J. Fluekiger, M. Caverley, L. Chrostowski, and N. A. F. Jaeger, Opt. Lett. **40**, 5578 (2015).
15. H. Okayama, Y. Onawa, D. Shimura, H. Yaegashi, and H. Sasaki, Opt. Express **23**, 19698 (2015).
16. H. Okayama, Y. Onawa, D. Shimura, H. Yaegashi, and H. Sasaki, Jpn. J. Appl. Phys. **56**, 042502 (2017).
17. H. Okayama, Y. Onawa, D. Shimura, H. Takahashi, H. Yaegashi, and H. Sasak, "Polarization rotator Bragg grating assisted wavelength selective polarization alignment," arXiv, arXiv:2112.05287 (2021).